Drainage in two-dimensional porous media: From capillary fingering to viscous flow

Christophe Cottin, Hugues Bodiguel,* and Annie Colin
Laboratory of the Future, UMR 5258, Université Bordeaux-1–CNRS, Rhodia, 178 Avenue du Docteur Schweitzer, 33608 Pessac Cedex, France

(Received 24 June 2010; published 28 October 2010)

This paper reports some experimental results on two-phase flows in model two-dimensional porous media. Standard microfluidic techniques are used to fabricate networks of straight microchannels and to control the throat size distribution. We analyze both the invasion mechanism of the medium by a nonwetting fluid and the drainage after the percolation for capillary numbers lying between 10^{-7} and 10^{-2}. We propose a crude model allowing a description of the observed capillary fingering that captures its scaling properties. This model is supported by numerical simulations based on a pore-network model. Numerical simulations and experiments agree quantitatively.

DOI: 10.1103/PhysRevE.82.046315 PACS number(s): 47.56.+r, 47.55.nb, 47.61.Jd, 47.53.+n

I. INTRODUCTION

An important class of "out of equilibrium" patterns occurs by forcing immiscible fluids in interconnected thin gap networks, a phenomenon frequently encountered in nature as well as in many manmade systems [1,2]. Illustrative examples include mineral processing, painting, construction engineering [3], printing [4], oil recovery [5], and soil mechanics. These fluid-fluid or fluid-gas displacements generate preferential flow pathways along one of the fluid flows, forming patterns ranging from compact to ramified and fractal. The formation and selection of these patterns are challenging problems in the field of nonequilibrium physics and central for many industrial applications. For instance, "tongues of water in oil" are a limiting factor in secondary oil recovery. One of the major difficulties in achieving a good understanding of preferential pathways in interconnected network is the large number of parameters potentially involved. These include the viscosity of the two fluids, the surface tension between them, the wetting properties, their respective flow rates, the topology of the network, and the considered length scales [6].

In the absence of viscous or gravity forces, the displacement (drainage) of a wetting fluid by a nonwetting fluid is solely governed by the capillary forces. They prevent the nonwetting fluid from spontaneously entering in a porous medium. It can only enter a throat (of radius R) when the pressure in the nonwetting fluid exceeds the pressure in the wetting fluid by a value P_c, the capillary pressure given by $P_c=2\gamma/R$, where γ is the surface tension [7]. Pressures in the nonwetting fluid and in the wetting one are uniform, and the displacement is governed by the pore size distribution. As a consequence, at the pore-network level, the front separating the two fluids advances by penetrating the largest pore throat accessible (i.e., the smallest capillary resistance). This process is successfully described by the invasion-percolation model [8,9].

In the presence of both viscous and capillary forces, the pressure field is not uniform anymore. The viscous forces modify the difference of pressure between the two fluids and promote the entrance of the invading fluid in smaller throat. In this case, the displacement is characterized by two dimensionless parameters: the capillary number $\mathrm{Ca}=V\eta_1/\gamma$, where V is the velocity of the injected fluid, η_1 is its viscosity, and γ is the surface tension, and the viscosity ratio $M=\eta_1/\eta_2$, where η_2 is the viscosity of the displaced fluid. For $M>1$, at low capillary numbers, the zone separating the two fluids includes a front with open structures on many length scales surrounded by two compact structures. As Ca increases, the front width decreases and leaves the place to a stable compact flow [10,11]. These two propagation mechanisms can be captured using concepts from gradient percolation (i.e., introducing a pressure gradient in the two fluids) [12–17]. For $M<1$, same picture holds for low capillary numbers. However, at high capillary numbers, viscous fingering causes an unstable displacement [17–19].

These phenomena were experimentally evidenced using micromodels of porous media which allow direct observations of the phases displacements [7,11,20,21]. However, at this stage, the comparison between experiments and theory remains usually qualitative or semiquantitative and is limited to the features of the patterns [14–16,22]. One of the difficulties to achieve a quantitative description is to account for the detailed features of the porous medium used. Microfluidic techniques offer the opportunity to fabricate micromodels with well-defined surface and geometrical features [21,23]. In this work, we revisit this problem using these to fabricate networks of straight microchannels with controlled size heterogeneities. Great care is brought to the control of the wetting properties. The features of the flow are determined from the movies of the filling of the micromodel. The measurement of the local velocities is compared to numerical simulations based on a network model [13,14] where the exact geometrical features of the micromodels are incorporated.

The paper is organized as follows. We present the experimental method in Sec. II. Then we discuss the experimental data in Sec. III. Section IV deals with a crude model to describe the invasion phase. In Sec. V, we report the results of numerical simulations and compare it to the experimental results. Finally, Sec. VI is devoted to the analysis of the filling behavior after percolation.

*hugues.bodiguel@u-bordeaux1.fr

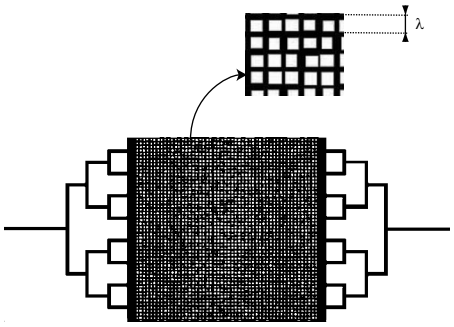

FIG. 1. Example of a mask used to grid ($\sigma/l=0.125$). The real size of the porous domain (the square lattice) is 1.3 cm.

II. EXPERIMENTAL METHOD

We performed experiments in microfluidic chips, made either of glass or polydimethylsiloxane (PDMS).

A. Design, microfabrication, and features of PDMS devices

Figure 1 displays the typical design used. It comprises three zones: the inlet, the porous domain, and the outlet. In order to impose a parallel pressure drop and a homogeneous filling of the cell, the inlet and the outlet have a treelike shape.

The porous geometry domain itself consists of a square lattice. The distance between two junctions λ is homogeneous and set to 250 μm. The width of the channels is not homogeneous; it is set randomly around a value w', with a normal distribution of standard deviation σ'_w without any spatial correlations.

These designs are printed on a transparency that will be used as a photomask. A SU8 2050 negative photoresist is spread on a silicon wafer and insolated through the previously described transparency. After resin development, a positive relief of photoresist on the silicon wafer is obtained. It serves as a mold. It is filled with a mixture of PDMS and curing agent and then heated during 45 min at 65 °C. The PDMS replica is then peeled from the mold and is sealed to a flat plate of glass previously coated with a thin layer of cured PDMS. The two surfaces are bounded together just after plasma exposure. The obtained surface after this bounding is hydrophilic and remains hydrophilic for more than 12 h. We will use in the following hydrophilic PDMS device. The experiments are conducted just after plasma exposure.

In this process, the features of the obtained channels networks are exactly the one designed on the photomask. The mean width w of the channels is thus equal to w'. The height of the microchannels h is set by the spin-coating process. Table I reports the features of the PDMS device that is used. Great care is devoted to the characterization of the throat size distribution. The standard deviation σ_w of the widths of the channels is set by the design and is equal to σ'_w. Microfabrication inaccuracies during the spin-coating process lead to a noncontrolled heterogeneity of the channel heights. The standard deviation σ_h of the channel heights is estimated using a profilometer and is approximately equal to 0.5 μm. The relative standard deviation ϵ of the curvature is given by $\epsilon = 2(\sigma_h/h^2+\sigma_w/w^2)/\mathcal{C}$, where $\mathcal{C}=2(1/h+1/w)$ is the mean curvature. The permeability of the porous media, defined as $k=Q\eta L/(N_w\lambda h\Delta P)$, is calculated from the theoretical hydrodynamic resistance of straight rectangular channels. In this formula Q is the flow rate of the injected fluid, ΔP is the corresponding drop of pressure between the inlet and the outlet of the device, and η is the viscosity of the Newtonian injected fluid.

TABLE I. Geometrical features of the devices: N_w is the number of junctions in the direction perpendicular to the pressure gradient, N_l is the number of junctions in the direction parallel to the pressure gradient, w is the mean width of the channels, σ_w is the standard deviation of the width of the channels, h is the mean height of the channel, σ_h is the standard deviation of the height of the channels, ϵ is the relative standard deviation of the curvature, ϕ is the porosity of the porous medium, and k is the permeability.

	a	b
Material	PDMS	Glass
$N_w \times N_l$	53×53	106×106
λ [a] (μm)	250	250
w' (μm)	80	38
w (μm)	80	90
h (μm)	50	25
σ_w (μm)	20	6
σ_h (μm)	0.5	0.1
ϵ	0.10	0.018
Coating		FluoroSi[b]
ϕ	0.52	0.69
k (Darcy)	12.0	2.55

[a]Wavelength of the square lattice.
[b]Trichloro(1H,1H,2H,2H perfluorooctyl)silane.

B. Design, microfabrication, and features of glass devices

In order to study various fluids, we have also made glass microdevices. The design of the photomask follows the procedure described in the previous section. Glass borosilicate wafers of thickness 500 μm were purchased from Sensor Prep Services. A 50 nm layer of chromium followed by a 100 nm of gold is evaporated on the wafer. These layers are sacrificial ones; they avoid hydrofluoric acid to attack the whole wafer. Then, we spin coat a positive photoresist (S1818) layer of approximately 2 μm. The resin is insulated through the masks described in the previous section and then developed. The gold and chromium layers are then removed in the insulated areas using oxydative solutions. Then, the wafer is immersed during 30 min in hydrofluoric acid from VWR (20% in water). The etching rate is about 1 μm/min.

Due to isotropic etching, the width of the channel w is larger than the width w' designed on the mask. We thus measure the width and the thickness of the channels after this step with a profilometer. For $w'=38$ μm we obtain channels having a width of about 90 μm after 30 min etching. We assume however that the standard deviation of the width remains close to the one set by the design. The standard devia-

TABLE II. Physical constants characterizing the three systems used.

	η_l (mPa s)	M	θ_a (deg)	θ_r (deg)	γ (mN/m)	S (mN/m)
Glass fluoroSi coating/water/dodecane	1	0.7	140	110	25	−2.9
Glass fluoroSi coating/water-glycerol/dodecane	14	10	140	110	25	−2.9
PDMS/FC40/water	3.4	3.4	160	140	44	−19

tion of the height measurement is roughly equal to 100 nm.

The last significant step of the fabrication of the chip concerns the thermal bonding of the two glass wafers: one with the chip engraved and the other one used as a lid. The two wafers are put 15 min in a mixture (50/50) of sulfuric acid and hydrogen peroxide at 50% in water, both solutions were purchased from Sigma Aldrich. They are then rinsed with distilled water and dried with a nitrogen flow, and put in contact together. They are then heated during 40 min at 705 °C and then 6 h at 523 °C (the glass transition of the material is 525 °C, according to the manufacturer). Glass chips were finally coated by trichloro(1H,1H,2H,2H perfluorooctyl)silane 97% (fluoroSi) to obtain oil wet surfaces. The chips were first cleaned with a hydrogen peroxide/acid sulfuric mixture and rinsed in distilled water. Then a flow of a solution of fluoroSi in FC40 oil from 3 M at 0.05% in volume is achieved in the micromodel at 10 μl/h during 30 min. It is followed by flows of toluene, chloroform, ethanol, and water for rinsing and then introduced for a few hours in a furnace at 65 °C. Table I gives the features of the glass microdevices that will be used in the following study.

C. Fluid and wetting properties

For all experiments, the displaced fluid is a wetting fluid and the invading fluid is a nonwetting one. The wetting fluid is either dodecane for glass surfaces or water in which a small amount of dye is dissolved for observation issues for the hydrophilic PDMS surface. The nonwetting is either water/glycerol (glass devices) or a fluorinated oil FC40 (PDMS devices).

The wetting properties of the systems are characterized by the spreading parameter $S=\gamma_{WS}-(\gamma_{OS}+\gamma)$, where γ_{WS}, γ_{OS}, and γ are the water/solid surface, the oil/solid surface, and the water/oil surface tensions, respectively. The liquid/liquid surface tensions were measured using the pendant drop method, while the liquid/solid ones are deduced from contact angle measurements of a water droplet in air and of an oil droplet in air on the solid surfaces (see Table II). Note that the colorant used for observation issues has tensioactive properties and lowers the water dodecane surface tension.

The two systems, water in dodecane on glass coated with fluoroSi and FC40 in water on PDMS, have a negative spreading parameter, and are thus in a *partial wetting* situation. It is rather difficult to measure the advancing and receding contact angles inside the chip. Using images of a water/oil meniscus inside a capillary tube that had undergone the same coating procedure, we were able to provide an estimate. For FC40 in water on hydrophilic PDMS, the advancing contact angle is 160° and the receding one is 140°. For water in dodecane on silanized glass, they are 140° and 110°. For both systems the contact angle hysteresis is rather high. Table II summarizes the wetting and viscous properties of the systems used.

D. Experimental procedure

Before each experiment, the micromodel is filled with the wetting fluid, using a syringe pump (Cetoni Nemesys). Then the invading phase is injected at a fixed flow rate in the range $2-10\,000$ μl/h. All the experiments are above the lowest flow rate for which the step-by-step motion of the syringe pump could be neglected, according to the manufacturer. The use of inlet channels that are thicker than the micromodel height ensures that the water phase does not penetrate into the porous domain before the inlet is filled. This enables us to define the time zero with a good accuracy to the time at which the first junction of the porous domain is invaded by the water phase.

A camera (JAI CM-200 GE) having a resolution of 1600×1200 and a frequency of 25 Hz with a 75 mm lens mounted on extension rings is used to acquire image sequences of the drainage in the micromodel. A homogeneous backlight is placed below the chip to obtain high-quality images, whose contrast is reinforced by an optical filter adapted to the spectrum of the colorant dissolved in the aqueous phase. The high contrast obtained allows a robust thresholding of the images (see the next section). On the images the water phase thus appears in dark gray, while the oil phase and the walls are brighter.

E. Data analysis

From the movies of the device filling, we determine the area of the invading phase as well as the position of all the menisci as a function of time. This allows us to estimate the applied capillary number and a mean local capillary number. The details of the procedure are given below.

Several analyses are performed on the images after the experiments. The images are first thresholded to isolate the invading phase. These images are directly used to measure the area A_1 of the invading phase. It linearly increases for $t<t_p$, where t_p is the percolation time, i.e., the time at which a continuous path is formed between the inlet and the outlet of the porous domain. It is thus verified that the syringe pump delivers a continuous and steady flow rate. The surface flow rate $q=dA_1/dt$ is measured. We checked that it is in agreement with Q/h, where Q is the volume flow rate imposed by the syringe pump and h is the height of the microchannel. The typical deviation is on the order of 5%. The

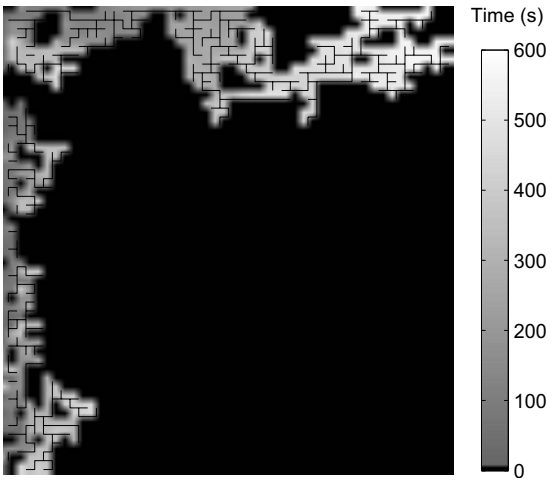

FIG. 2. Example of data analysis for an experiment made in grid a with $Ca_i = 4.3 \times 10^{-7}$. The gray scale represents the time at which the nodes have been invaded (the darker the sooner), and the small lines indicate the path followed by the invading fluid.

value of q is used to calculate the imposed capillary number of the experiment, Ca_i, which allows the comparison between the different fluids used. For single-phase flow in a regular grid, the flow rate theoretically vanishes inside the channels perpendicular for symmetry reasons, and the mean velocity inside the parallel ones is then $v_i = Q/N_w S = q/N_w w$, where N_w is the number of the channels parallel to the pressure gradient and S is their cross section. We define the imposed capillary number as $Ca_i = \eta_1 v_i/\gamma$, where η_1 stands for the viscosity of the invading phase. The oil saturation S_o is also deduced from the thresholded image sequence, $S_o = 1 - A_1/\phi A_0$, where ϕ is the porosity of the micromodel calculated from the mask and A_0 is the total area of the porous domain.

Then the grid used for the mask is adjusted to the images, in order to label each junction and each node. A node is the place where four junctions meet. To estimate the local velocity field, we follow the procedure described bellow. We measure the time t_m at which the node labeled m is invaded by the water phase. We deduce the path followed by the water by testing the four possible paths to the neighboring nodes. This allows us to find the node n from which the water comes. In more than 95% of the analyzed data, menisci cover a distance l smaller than λ between two successive pictures. This algorithm allows us to reconstruct the time-resolved menisci paths of the experiment. An example is shown in Fig. 2.

We define a local velocity $v_{mn} = \lambda/(t_m - t_n)$ and a corresponding local capillary number $Ca_{mn} = \eta_1 v_{mn}/\gamma$, where m and n are neighboring nodes. The largest velocity that could be measured by this method due to temporal sampling of the camera is 6.2 mm/s. Averaging these data on space and time, we calculate a mean local capillary number $\langle Ca_l \rangle$. It has been verified that this average does not vary significantly with time. When the invading front is not sharp but exhibits a fingering instability, $\langle Ca_l \rangle$ and Ca_i are not equal. They are linked by the number of selected paths N_s, defined by $Ca_i = \langle Ca_l \rangle N_s/N_w$, where N_w is the number of channels along the width of the grid, and where $N_s \leq N_w$. When there is no fingering (perfect sweeping of the device), $N_s = N_w$ and thus $\langle Ca_l \rangle = Ca_i$.

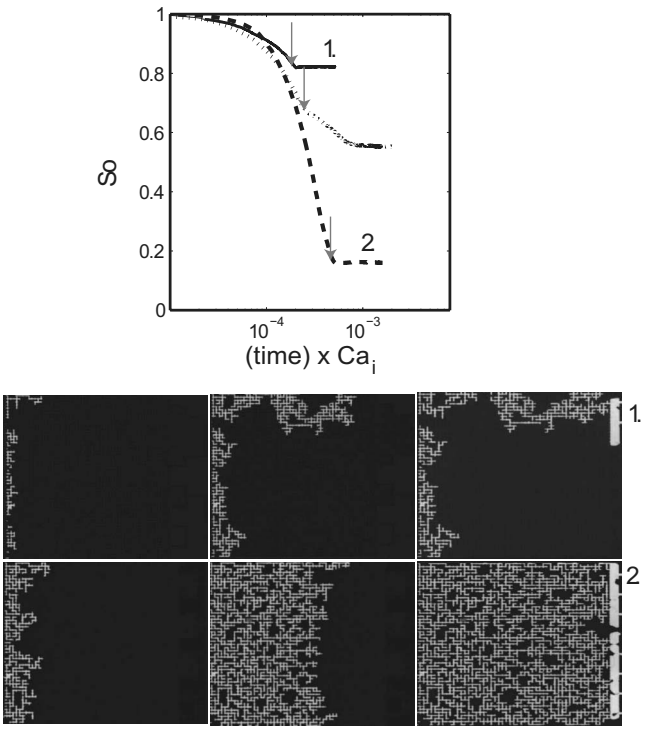

FIG. 3. The injected fluid is fluorinated oil; the captured fluid is water. Experiments are performed on a hydrophilic PDMS grid (grid a). Top figure: evolution of the captured fluid saturation as a function of time multiplied by the applied capillary number Ca_i. From top to bottom $Ca_i = 9 \times 10^{-7}$ (1), 1.85×10^{-5}, 2.4×10^{-4} (2). Bottom figures: typical pictures during the invasion process at two different applied capillary numbers (labeled 1 and 2 in the top figure). For the sake of clarity, the contrast of the picture has been inversed. The darkest fluid is the injected fluid.

III. EXPERIMENTAL RESULTS

We study systems in partial wetting situation, which are fluorinated oil pushing water in hydrophilic PDMS device ($M = 3.4$) and water-glycerol mixtures pushing dodecane in the fluoroSi glass device ($M = 0.7$ and $M = 10$). Examples of initially captured fluid saturation as a function of time and typical pictures taking during the sweeping process are displayed in Fig. 3 for different applied capillary numbers. The saturation curves exhibit two steps. During the invading step, the injected fluid flows in the device and reaches the outlet. For low applied capillary numbers an open structure grows and fills the micromodel (see the first sequence in Fig. 3). The size of the clusters trapped behind the advancing front decreases when the applied capillary number increases (see the second sequence in Fig. 3). For higher applied capillary numbers, the growing structure is more compact. As soon as the injected fluid reaches the outlet, (i.e., at the percolation time), the sweeping efficiency of the captured phase drops dramatically. In some experiments (see the upper and lower curves in Fig. 3), we even note that the saturation remains

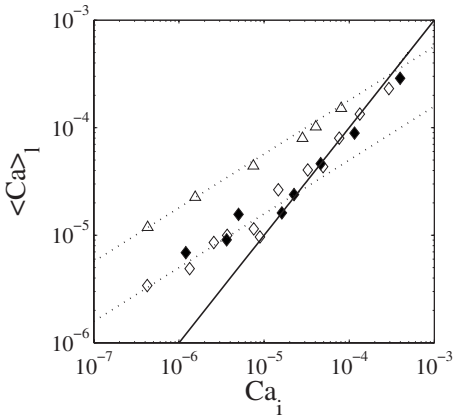

FIG. 4. Variations of the measured mean local capillary number $\langle Ca_l \rangle$ as a function of the imposed one Ca_i. The full lozenges (♦) correspond to experiments where the water-glycerin mixture is pushing dodecane in grid b, the empty lozenges (◇) correspond to water pushing dodecane in grid b, and the triangles (△) correspond to fluorinated oil pushing water in grid a. The full line corresponds to $\langle Ca_l \rangle = Ca_i$. The dotted lines correspond to $\langle Ca_l \rangle = A\sqrt{Ca_i}$, where the numerical constant A equals from the top to the bottom to 1.8×10^{-2} and 5×10^{-3}.

perfectly constant after percolation. In the other cases (see the middle curve in Fig. 3), the sweeping of the captured phase decreases strongly after percolation before vanishing. We note that the higher the applied capillary number, the better the global sweeping efficiency.

Let us now describe more quantitatively the invading step. As explained in the experimental section, we measure the mean local capillary $\langle Ca_l \rangle$ number before the percolation and compare it to the applied capillary number Ca_i. Figure 4 displays three sets of data corresponding to three couples of fluid having different viscosity ratios inside two different micromodels. The data evidence two regimes. For low Ca_i, the mean local capillary number before percolation is higher than the applied one and is well described by the relation $\langle Ca_l \rangle \propto Ca_i^{1/2}$. As explained in the experimental section, the ratio of these two quantities corresponds to the ratio between the total number of channels N_w and the number of selected paths N_s. This simply means that the flow occurs in a few channels at a time and reflects the fingering that is seen in the images displayed in Fig. 3. This regime will be called the capillary regime in contrast to the viscous regime that is observed at higher applied capillary numbers where $\langle Ca_l \rangle$ is equal to Ca_i. Indeed, in this regime, flow occurs in all the channels simultaneously. As shown in Fig. 4, the transition from the viscous regime to the capillary one occurs at a capillary number that depends on the system (size heterogeneity, contact angle, and channel dimensions). This point will be discussed in the following sections.

We finally study the percolation phase. Since there is a low sweeping after percolation, the value of the oil saturation in the final state is controlled by the invasion process. Figure 5 displays the evolution of the captured phase saturation as a function of the applied capillary number. It decreases when the applied capillary number is increased. We note that for low capillary numbers, the sweeping efficiency is very low.

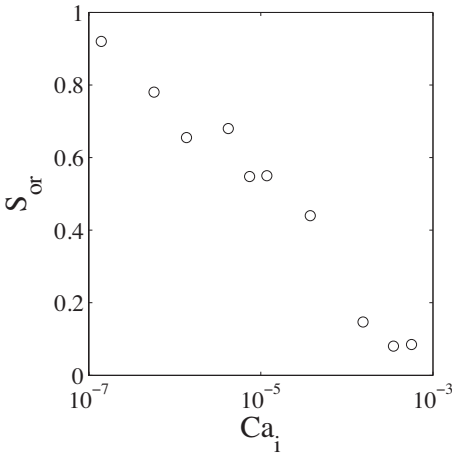

FIG. 5. Variation of the residual oil saturation at the percolation S_{o_r} as a function of the applied capillary number Ca_i. Data correspond to the water-dodecane system in grid b.

Large oil clusters remain trapped after the percolation. Their maximal size is on the order of the width of the porous domain for the lowest capillary numbers tested and decreases for higher values of Ca_i. We report in Fig. 6 an estimation of the maximum cluster size as a function of the applied capillary number. It follows roughly a −0.5 power law, although the scatters in the data (due to poor statistics) do not allow us to conclude on the exponent. In the following, it will be shown that this result is however consistent with the local velocity measurements in the capillary regime reported in Fig. 4.

IV. CRUDE MODEL TO CAPTURE THE INVASION PROCESS

In order to understand the previous data, let us go back to the invasion-percolation model in presence of viscous forces.

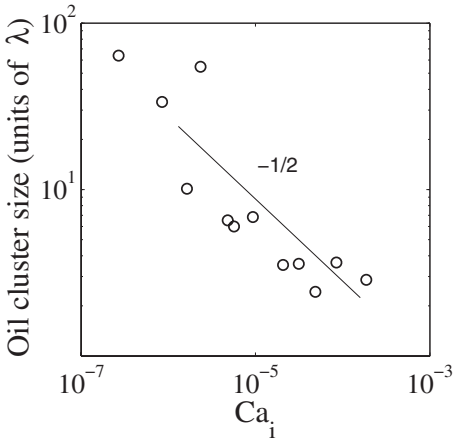

FIG. 6. Maximum size (in the pressure gradient direction) of remaining oil clusters as a function of Ca_i for the water-dodecane system in grid b. The size is reported in numbers of junctions. The line corresponds to a slope of −1/2. Note that the data dealing with number of λ greater than 20 correspond to huge clusters where finite-size effect could play an important role.

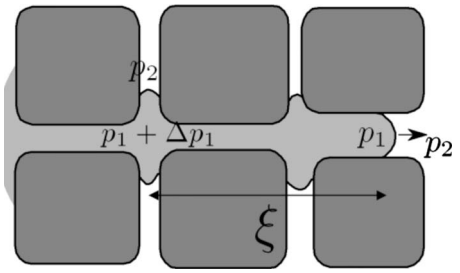

FIG. 7. Scheme of the pressure field in the case of partial wetting. The colored phase is the invading fluid.

As described in the introduction, in the absence of viscous forces or at very low capillary number, the nonwetting fluid enters little by little the largest of the accessible throats since the flow is driven by the capillary pressure only. At each time step, only the meniscus located in the largest throat advances. When viscous forces are considered (i.e., for small but nonzero capillary numbers) a pressure gradient appears in the invading and in the captive fluid. The corresponding viscous drop of pressure induced by the viscous forces may become on the order of magnitude of the difference of Laplace pressures between a small throat and a large one. Then the invasion-percolation mechanism is no longer strictly valid, and the invading fluid also enters smaller throats, provided that these are located upstream, beyond a distance ξ. This distance represents the width of the front. Although the invasion-percolation theory with viscous forces has been developed using different approaches [12,17], we propose in the following a greatly simplified model, based on the arguments recalled above, and that is sufficient to account for the experimental results reported in the previous section.

Let us assume that the pressure field inside the displaced phase remains uniform in the region of the advancing meniscus the front and equals p_2. This assumption is straightforward when the invading fluid has a greater viscosity than the captured one ($M>1$) and may remain valid even for $M \lesssim 1$ due to the geometry of front. Considering, as sketched in Fig. 7, a moving meniscus advancing in a large throat, the pressure p_1 in the advancing phase close to the meniscus is given by the local capillary pressure, i.e., $p_{1_m} - p_2 = p_{c_m}$. In the limit of low capillary numbers, we could neglect variations of the meniscus curvature due to viscous forces. Inside the invading phase, the pressure increases upstream due to viscous forces. At a distance ξ beyond the moving meniscus the pressure increment reads $\Delta p_1 = \alpha \xi \eta_1 V / h^2$, where V is the velocity of the moving meniscus and α is a numerical constant that depends on the aspect ratio of the channels; $\alpha = 12$ for vanishing values of h/w. The distance ξ is then defined by the distance at which the blocked menisci could enter the throats, which implies that the viscous pressure increment in the invading phase overcomes the Laplace pressure difference $p_{c_m} - p_{c_b}$. This condition reads in average $\Delta p_1 = f \epsilon p_c = f \epsilon \gamma |\cos\ \theta_a| \mathcal{C}$ [24], where ϵ is the relative standard deviation of the curvature due to channel dimensions and f is a numerical factor that should be on the order of unity and that accounts for an effective standard deviation. Thus, ξ is given by

$$\xi \simeq \frac{f \epsilon p_c h^2}{\alpha \eta_1 V} = \lambda \frac{\Gamma f \epsilon |\cos\ \theta_a|}{\mathrm{Ca}_l}, \tag{1}$$

where Ca_l is the local capillary number, calculated from the velocity of the moving meniscus, which is experimentally measured. In this equation, we have introduced a geometrical constant Γ that depends on the geometry of the channels. It is defined by $\Gamma = \mathcal{C} h^2 / \alpha \lambda$. For our models of porous media, Γ is equal either to 2.2×10^{-2} (grid b) or to 5.4×10^{-2} (grid a).

Then, let us assume that the width of the front ξ is also the mean distance between two moving meniscus. Volume conservation of the invading liquid allows us to relate the local capillary number with the global capillary number Ca_i that is imposed and reads $\xi/\lambda \simeq \langle \mathrm{Ca}_l \rangle / \mathrm{Ca}_i$. Using Eq. (1), we obtain the following predictions for the width of the front:

$$\xi = c' \lambda \sqrt{\frac{\epsilon \Gamma |\cos\ \theta_a|}{\mathrm{Ca}_i}}, \tag{2}$$

or alternatively for the mean local capillary number

$$\langle \mathrm{Ca}_l \rangle = c \sqrt{\epsilon \Gamma |\cos\ \theta_a| \mathrm{Ca}_i}, \tag{3}$$

where the constants c and c' are numerical factors that account for both f and the scaling argument linking ξ and $\langle \mathrm{Ca}_l \rangle$.

This regime holds for capillary numbers where the correlation length ξ is larger than λ, the distance between two nodes. For higher capillary numbers ($\mathrm{Ca}_i > c^2 \epsilon \Gamma |\cos\ \theta|$), $\langle \mathrm{Ca}_l \rangle = \mathrm{Ca}_i$. It also implies that ξ is lower than the width of the micromodel; for very low capillary numbers, there is only one moving meniscus simultaneously, and thus we expect $\langle \mathrm{Ca}_l \rangle = N_w \mathrm{Ca}_i$ when $\mathrm{Ca}_i < c^2 \epsilon \Gamma |\cos\ \theta| / N_w^2$. This last regime is not observed in the data reported in Fig. 4, but should exist in a smaller grid or at lower capillary numbers.

This crude model captures well the experimental data. Indeed, the mean local capillary number varies as a power law of the applied capillary number with an exponent equal to 0.5 (see Fig. 4) which is the value predicted by the model. We do not directly measure ξ to test Eq. (2) because of too poor statistics, but Frette *et al.* reported front width measurements during the drainage of viscosity-matched liquids that are also consistent with our description; indeed, they found that $\xi \propto \mathrm{Ca}_i^{-0.6(\pm 0.2)}$ [11]. Since the viscous pressure gradient is directly proportional to the local capillary number, our model leads, in the capillary regime, to a relative permeability for the nonwetting phase that scales like $\mathrm{Ca}_i^{0.5}$. One may note that this result corresponds exactly to the one obtain recently by Tallakstad *et al.* in steady-state experiments [25], when the viscous dissipation is negligible in one of the two phases.

Equation (3) also predicts—up to an unknown factor c—the dependence of the local capillary number as a function of the capillary pressure heterogeneity and the geometry of the throats. Although these are not varied systematically, the two devices used allow us to test this prediction since the values of ϵ, Γ, and $\cos\ \theta_a$ are well defined. Experiments performed on the water/dodecane system, on the water-glycerol/dodecane system, and on the fluorinated oil/water system correspond to prefactors c of 5×10^{-3}, 5×10^{-3}, and 1.8

$\times 10^{-2}$, respectively. According to Eq. (3), these should be 1.7×10^{-2}, 1.7×10^{-2}, and 7.1×10^{-2}, respectively. Even though these values do not agree well, we should note that they are consistent when using an empirical value for the coefficient c of 0.27. In the following section, we will present numerical simulation allowing a quantitative description of these results.

V. NUMERICAL SIMULATIONS

In order to account for this numerical coefficient, we performed numerical simulations using a crude version of standard pore-network models (PNMs). In these simulations, the pressure field is solved during the invasion which allows us to displace step by step the menisci for which the pressure drop between two nodes exceeds the local capillary pressure, set randomly with a relative standard deviation ϵ. We used for the simulation a geometry that is exactly that of the micromodels used for the experiments. The algorithm used for the simulation is a crude version of standard PNM that has been widely used for the last two decades (see, for examples, Refs. [13,15,22,26]).

A. Description of the PNM

As in standard PNM, there is no volume associated with nodes, and the throats between nodes are channels of heterogeneous width, having a hydrodynamic conductance given by $g_{ij}=w_{ij}h^3/\alpha(w_{ij}/h)\eta_1\lambda$ if the channel is occupied by the displacing fluid and Mg_{ij} otherwise. The numerical factor $\alpha(w_{ij}/h)$ that depends on the aspect ratio of the rectangular channels is calculated according to the analytical expression reported in Ref. [27]. Similarly to the experimental geometry, the widths of the channels w_{ij} are set randomly using a Gaussian distribution of mean value w and of standard deviation σ_w. The capillary pressure P_c thus exhibits a standard deviation ϵ, given by $\epsilon=2\sigma_w/w^2\mathcal{C}$. If there is a meniscus located between nodes i and j, the conductance is set to zero when $P_i-P_j<P_{c_{ij}}$, where $P_{c_{ij}}=\gamma\mathcal{C}_{ij}|\cos\theta_a|$ is the local capillary pressure inside the channel ij. In that case, the meniscus is blocked; otherwise, it is moving (we only consider advancing menisci).

The flow rate q_{ij} between two neighboring nodes is then given by

$$q_{ij}=\nu'_{ij}g_{ij}M'_{ij}(P_i-P_j-\nu_{ij}P_{c_{ij}}), \tag{4}$$

where $\nu_{ij}=0$ if there is no meniscus between i and j, $\nu_{ij}=1$ if the node j is occupied by the displaced fluid and the node i is occupied by the displacing one, and $\nu_{ij}=-1$ in the opposite case. In the previous equation, $\nu'_{ij}=1$, except for blocked meniscus where $\nu'_{ij}=0$. $M'_{ij}=M$ if the channel is occupied by the displaced fluid and $M'_{ij}=1$ otherwise.

At each node, volume conservation leads to

$$\sum_j q_{ij}=0, \tag{5}$$

where the summation is made on the neighboring nodes. Similarly to the experiments, we consider a square lattice, with for boundary conditions a uniform pressure ΔP on the left side, uniform pressure set to zero on the right side, and no flux on the other sides. For the initial condition, the left column is occupied by the displacing fluid and the other nodes of the lattice are occupied by the displaced fluid. Equations (4) and (5) form a complete linear system of equations that could be solved easily. However, since we aim to perform experiments at an imposed flow rate rather than an imposed pressure, we use a small approximation to simplify the calculation. We replace in Eq. (4) the capillary pressure with the mean capillary pressure $\langle P_{c_m}\rangle$ of the moving menisci. We then define the viscous pressure field P_v by $P_{v_i}=P_i$ if the node i is occupied by the displaced fluid and $P_{v_i}=P_i-\langle P_{c_m}\rangle$ otherwise. Substituting P with P_v in Eq. (4) reduces the equation to

$$q_{ij}=\nu'_{ij}g_{ij}M'_{ij}(P_{v_i}-P_{v_j}). \tag{6}$$

This approximation thus leads to a linear relation between the flow rate Q and the viscous pressure P_v. The equations are solved with $\Delta P_v=1$ and the results are then rescaled to obtain the desired flow rate.

Since we only want to obtain a crude model that could described the experiments, we use a rough time step assuming that all the moving menisci have the same velocity, simply given by $Q/N_s\Sigma$, where N_s is the number of moving menisci and Σ is the mean cross-section area of the channels. With such an approximation, all the menisci that verify the moving criterion at time t_i reach the next node at time t_{i+1}. This last approximation reduces greatly the computing time. It leads however to undesirable and artificial oscillations when looking at N_s as a function of time, especially for high Ca_i. We thus focus on the mean value, assuming that is it not much altered by these oscillations.

Finally, the sequence of the algorithm is the following:

(1) The viscous pressure field P_v is solved using Eqs. (5) and (6).

(2) The viscous pressure field is rescaled to obtain the desired flow rate, and the mean capillary pressure of the moving menisci $\langle P_{c_m}\rangle$ is added to the nodes containing the displacing fluid.

(3) For each meniscus separating the two phases, the moving criterion $P_i-P_j>P_{c_{ij}}$ is checked to determine the moving and blocked menisci. The number N_s of moving menisci is stored in order to compute the mean local capillary number $\langle \mathrm{Ca}_l\rangle$.

(4) The conductances of the channels containing the menisci are set either to zero for blocked meniscus or to g for moving ones.

(5) The nodes reached by the moving menisci are updated with the displacing fluid.

This sequence is repeated until the invading fluid reaches the right side of the square lattice.

B. Comparison between experimental and numerical results

One of the outputs of the simulation is the number N_s of menisci that move simultaneously, which is directly linked to the local capillary number by $\langle \mathrm{Ca}_l\rangle=\mathrm{Ca}_i N_w/N_s$. Equation (3) suggests that the relevant parameter is not the capillary num-

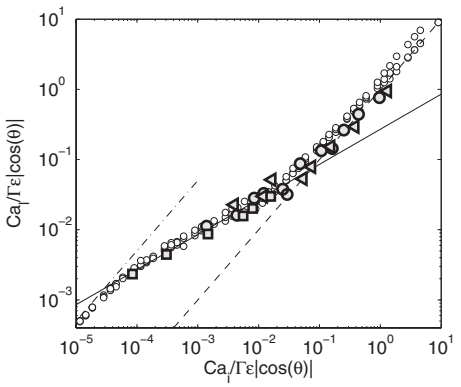

FIG. 8. Modified local capillary number $\widetilde{\langle \mathrm{Ca}_l \rangle} = \langle \mathrm{Ca}_l \rangle / \Gamma \epsilon |\cos \theta_a|$ as a function of the imposed one $\widetilde{\mathrm{Ca}_i}$. The numerical results (small circles) are plotted together with the experimental data reported in Fig. 4 (big symbols). The dashed line is $\widetilde{\langle \mathrm{Ca}_l \rangle} = \widetilde{\mathrm{Ca}_i}$, holding for the viscous regime; the solid line is $\widetilde{\langle \mathrm{Ca}_l \rangle} = 0.27\sqrt{\widetilde{\mathrm{Ca}_i}}$, holding for the capillary regime; and the dashed-dotted line is $\widetilde{\langle \mathrm{Ca}_l \rangle} = N_w \widetilde{\mathrm{Ca}_i}$ holding for the finite-size regime at ultralow Ca_i. The simulation parameters are Ca_i (varied between 10^{-8} and 10^{-2}), ϵ (varied between 5×10^{-3} and 0.1), Γ (varied between 10^{-2} and 0.1), M (varied between 0.7 and 10), $\cos\theta_a = -1$, and $N_w = 50$.

ber, but a modified one Ca defined by $\widetilde{\mathrm{Ca}} = \mathrm{Ca}/\Gamma\epsilon|\cos\theta_a|$. The latter is used in Fig. 8 where the modified local capillary number is plotted as a function of the imposed one. All the points obtained through the numerical simulations collapse on a single curve. We evidence three regimes. For ultralow values of $\widetilde{\mathrm{Ca}_i}$, $\widetilde{\langle \mathrm{Ca}_l \rangle} = N_w \widetilde{\mathrm{Ca}_i}$. In this regime, the width of the front is larger than the size of the porous media. This regime thus corresponds to a finite-size effect regime. For higher values of $\widetilde{\mathrm{Ca}_i}$, the front size becomes smaller than the porous media size, and we enter in the capillary regime characterized by a power law with an exponent close to 0.5. As suggested, the boundary between the finite-size regime and the capillary one depends on the size of the micromodel. High values of $\widetilde{\mathrm{Ca}_i}$ correspond to the viscous regime, where $\widetilde{\langle \mathrm{Ca}_l \rangle} = \widetilde{\mathrm{Ca}_i}$.

Since in the simulations the parameters ϵ and Γ could be varied independently and on a wider range than in the experiments, the numerical results validate Eq. (3) for all of its dependencies in the tested range. We have also reported in Fig. 8 the experimental data presented in the previous sections. Their agreement with the numerical results is beyond the uncertainty of the data. In particular, the numerical simulation predicts quantitatively the crossover between the viscous and the capillary regimes. This validates the value of the empirical numerical factor c of 0.27 ($\pm$0.02). The crossover happens for $\widetilde{\mathrm{Ca}} = c^2 = 7.3\times10^{-2}$.

The very good collapse in Fig. 8 suggests that the approximations made in the PNM do not alter the final results when looking at the mean value of the number of selected paths. This quantity appears to be robust and to reach rapidly a steady state, in both experiments and simulations. An analysis of the fluctuations during the invasion would in contrast require us to remove the approximations made (as in Ref. [13]), at the price of a great increase in the computing time.

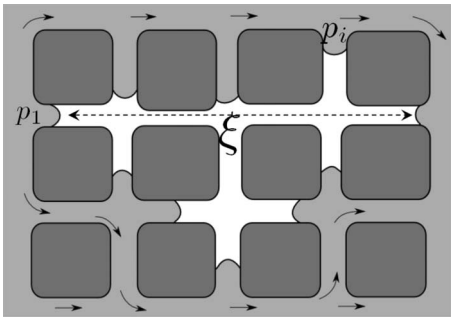

FIG. 9. Scheme of a trapped cluster. The colored fluid is the injected fluid. The arrows indicate the flow direction.

VI. DRAINAGE AFTER THE PERCOLATION

Let us finally discuss the evolution of the filling after the percolation. After percolation the clusters trapped during the invasion process are stable, and a freezing of the structure of the invading fluid is observed after the percolation. The analysis of the size of the clusters is straightforward and follows the previous arguments. Since these clusters are formed during the invasion, their size is similar to the width of the front, which—according to Eq. (2)—should scale like $\mathrm{Ca}_i^{-0.5}$. The experimental data, reported in Fig. 6 are consistent with such a power-law variation. The freezing of the structure of the invading fluid that is observed after the percolation is more striking. One may wonder why the clusters remain definitively trapped. It is easy to note that in partial wetting situations these structures are disconnected. The single way to sweep the trapped fluid is to displace the clusters.

Let us analyze in detail the conditions required for the displacement of a cluster. A cluster moves forward only if the pressure difference between the two points 1 and i, $p_1 - p_i = \Delta P_{1i}$, located in the invading phase exceeds the local advancing capillary pressure, given by $\gamma|\cos\theta_a|\mathcal{C}_1 - \gamma|\cos\theta_r|\mathcal{C}_i$, where θ_a is the advancing contact angle and θ_r is the receding contact angle. Symmetrically, a cluster could move backward if ΔP_{1i} is below $\gamma|\cos\theta_r|\mathcal{C}_1 - \gamma|\cos\theta_a|\mathcal{C}_i$. Two distinct points i and 1 located on the borders of the clusters bear a drop of pressure due to the flow in the invading fluid, $\Delta P_{1i} = \alpha\eta V L_{1i}/h^2$, where L_{1i} is the distance between locations 1 and i. The stability criterion, sketched in Fig. 9, is thus given by

$$\frac{\mathcal{C}_i}{\beta} + \frac{f\epsilon\mathcal{C}L_{1i}}{\xi} < \mathcal{C}_1 < \beta\left(\mathcal{C}_i + \frac{f\epsilon\mathcal{C}L_{1i}}{\xi}\right), \tag{7}$$

where $\beta = \cos\theta_a/\cos\theta_r$. Since the curvatures $\mathcal{C}_1$ and $\mathcal{C}_i$ could only vary in a limited range, it is not easy at first sight to tell if this criterion may be filled or not. The menisci located on the borders of the clusters are however particular. During the invading step, they have not been filled. This suggests that the menisci may find locations in the junctions where their curvatures check:

$$\mathcal{C}_1 = \mathcal{C}_i \frac{\cos(\theta_i)}{\cos(\theta_1)} + \frac{f\cos(\theta_a)\epsilon \mathcal{C} L_{1i}}{\xi \cos(\theta_1)}, \tag{8}$$

where θ_1 and θ_i are comprised between θ_r and θ_a. Locations following Eq. (8) clearly fill the criterion of Eq. (7), implying that the oil clusters are stable in partial wetting situations. Moreover, due to contact angle hysteresis, many other equilibrium positions in the vicinity of the one defined by Eq. (8) exist. This suggests that the clusters are going to be stable toward pressure fluctuations and explains the absence of sweeping efficiency after the percolation.

VII. CONCLUSION AND OUTLOOK

In this work, we revisit the drainage of a fluid by a more viscous one in porous media. We perform experiments in microdevices prepared using standard lithography techniques with controlled throat size distribution. Experiments evidence the role of the viscous forces during the invasion process and their competition with the capillary force heterogeneities. At very low applied capillary number, the invading liquid flows through a single channel at the time and build a very open structure. Increasing the applied capillary number induces an increase in the role of the viscous forces. Due to the geometry of the structure, the viscous pressure gradient in the oil phase is very small. At the opposite, the pressure inside the advancing meniscus increases as a function of the distance to the meniscus and, at a given distance from the front, becomes greater than the Laplace pressure required to enter a small throat. This induces a modification of the invasion-percolation process. All the throats upstream this distance are filled by the oil, unless they are trapped. This argument leads to a crude model linking the applied capillary number calculated by using the viscosity of the injected phase to the number of selected path. The local capillary number is predicted and observed to scale like $\mathrm{Ca}^{0.5}$, which means that the correlation length of the invasion process is proportional to $\mathrm{Ca}^{-0.5}$.

Moreover, our analysis suggests that it is a modified capillary number $\widetilde{\mathrm{Ca}}=\mathrm{Ca}/\Gamma\epsilon|\cos\,\theta_a|$ that solely governs the invasion, taking into account the pore throat geometry and the size heterogeneity. If our model accounts for the experiments up to an unknown factor, we obtain a quantitative agreement using numerical simulation based on a pore-network model. Indeed, we report a master curve in the parameter plane $(\widetilde{\mathrm{Ca}_i}, \widetilde{\langle \mathrm{Ca}_l \rangle})$ where experimental and numerical results collapse. It shows that the capillary fingering occurs below $\widetilde{\mathrm{Ca}_i}=0.1$.

After the percolation, the structure of the invading fluid is very rapidly frozen. The inlet and the outlet of the device are bypassed by a continuous path of water where no meniscus is present. The viscous drop of pressure is too low to sweep the clusters. Contact angle hysteresis promotes the stability of the trapped structure.

This work allows us to set quantitatively the basis of the drainage process. It opens the road to the analysis of the role of the features of the injected fluid. The outlook deals with the analysis of the wetting and rheological properties of the invading fluid on the invasion and after percolation phase.

ACKNOWLEDGMENTS

The authors thank Rhodia and Région Aquitaine for financial support and appreciate valuable discussions with Mikel Morvan and Max Chabert.

[1] A. Bajan, *Shape and Structure: From Engineering to Nature* (Cambridge University Press, Cambridge, England, 2000).
[2] F. A. L. Dullien, *Porous Media, Second Edition: Fluid Transport and Pore Structure*, 2nd ed. (Academic Press, New York, 1991).
[3] N. R. Morrow and F. G. MacCaffrey, in *Wetting, Spreading and Adhesion*, edited by J. G. Padday (Academic, New York, 1978), pp. 289–319.
[4] J. Rosinski, Am. Ink. Maker **71**, 40 (1993).
[5] M. Cil and J. C. Reis, J. Pet. Sci. Eng. **16**, 61 (1996).
[6] J. P. Stokes, D. A. Weitz, J. P. Gollub, A. Dougherty, M. O. Robbins, P. M. Chaikin, and H. M. Lindsay, Phys. Rev. Lett. **57**, 1718 (1986).
[7] R. Lenormand and C. Zarcone, Phys. Rev. Lett. **54**, 2226 (1985).
[8] P. G. De Gennes and E. Guyon, J. Mec. **17**, 403 (1978).
[9] D. Wilkinson and J. F. Willemsen, J. Phys. A **16**, 3365 (1983).
[10] R. Lenormand, Proc. R. Soc. London, Ser. A **423**, 159 (1989).
[11] O. I. Frette, K. J. Måløy, J. Schmittbuhl, and A. Hansen, Phys. Rev. E **55**, 2969 (1997).
[12] D. Wilkinson, Phys. Rev. A **34**, 1380 (1986).
[13] E. Aker, K. J. Måløy, and A. Hansen, Phys. Rev. E **58**, 2217 (1998).
[14] E. Aker, K. J. Måløy, and A. Hansen, Phys. Rev. E **61**, 2936 (2000).
[15] M. Ferer, G. S. Bromhal, and D. H. Smith, Phys. Rev. E **71**, 026303 (2005).
[16] M. Ferer, G. S. Bromhal, and D. H. Smith, Phys. Rev. E **76**, 046304 (2007).
[17] B. Xu, Y. C. Yortsos, and D. Salin, Phys. Rev. E **57**, 739 (1998).
[18] G. Løvoll, Y. Meheust, R. Toussaint, J. Schmittbuhl, and K. J. Måløy, Phys. Rev. E **70**, 026301 (2004).
[19] M. Ferer, C. Ji, G. S. Bromhal, J. Cook, G. Ahmadi, and D. H. Smith, Phys. Rev. E **70**, 016303 (2004).
[20] M. A. Theodoropoulou, V. Sygouni, V. Karoutsos, and C. D. Tsakiroglou, Int. J. Multiphase Flow **31**, 1155 (2005).
[21] V. Berejnov, N. Djilali, and D. Sinton, Lab Chip **8**, 689 (2008).
[22] R. Lenormand, E. Touboul, and C. Zarcone, J. Fluid Mech. **189**, 165 (1988).
[23] D. Crandall, G. Ahmadi, D. Leonard, M. Ferer, and D. H. Smith, Rev. Sci. Instrum. **79**, 044501 (2008).

[24] We limit ourselves to small heterogeneities of standard deviations lower than the throat size.

[25] K. T. Tallakstad, H. A. Knudsen, T. Ramstad, G. Løvoll, K. J. Måløy, R. Toussaint, and E. G. Flekkøy, Phys. Rev. Lett. **102**, 074502 (2009).

[26] N. Martys, M. Cieplak, and M. O. Robbins, Phys. Rev. Lett. **66**, 1058 (1991).

[27] N. A. Mortensen, F. Okkels, and H. Bruus, Phys. Rev. E **71**, 057301 (2005).